Int J Heat Mass Transfer Vol 33 No 11, pp 2545–2563 1990
Printed in Great Britain

0017–9310/90 $3 00 + 0 00

Steady-state natural convection with phase change

WEI SHYY and MING-HSIUNG CHEN

Department of Aerospace Engineering, Mechanics and Engineering Science, University of Florida, Gainesville, FL 32611, U S A

(*Received* 26 *September* 1989 *and in final form* 17 *January* 1990)

Abstract—Natural convection significantly affects the thermofluid transport processes for a material experiencing phase change In the present work, steady-state solutions of the convection and associated momentum and energy transfer are computed by considering the solid, liquid, and mushy zones simultaneously Finite-volume computational techniques, including the use of non-orthogonal curvilinear coordinates, second-order discretization, adequate number of nodal points, and adaptive grid solution method are utilized for wide ranges of Rayleigh, Prandtl, and Stefan numbers It is found that the size and strength of the convection cell, as well as the location and shape of the phase boundaries are all strongly dependent on the combination of the above controlling parameters, as well as the temperature range governing the existence of the mushy zone A systematic presentation of the effect of those factors on the transport characteristics is made to delineate the physical mechanisms responsible for the phase change process

1. INTRODUCTION

MELTING and solidification problems are important in material processing, including the synthetic production of alloy and crystal. Phase change processes necessarily proceed with temperature gradients in the liquid phase which can couple with the gravitational force to produce buoyancy-induced convection. The interaction of convection in the melt along with the solidification process can have a very strong effect on the resulting structure and performance of the material [1, 2] Extensive efforts have been devoted to developing suitable physical models and computational techniques to better understand the transport processes in the presence of phase change In terms of the physical models, different treatments can be made to account for the existence of the mushy zone between the solidus and the liquidus phases [1, 3, 4] There are also relative advantages and disadvantages between adopting the temperature and the enthalpy as the primary variables in the energy equation [4–6]. With regard to the computational techniques, both the finite difference/finite volume [7–10] and the finite element [11–13] formulations have been utilized to study the solidification problem with the inclusion of the convection effect

In order to accurately solve the governing differential equation with the controlling parameters in the ranges of practical interest, the calculations are extremely demanding in resource The wide disparity of length scales for momentum, energy, and solute, as well as the unknown interface location generally requires supercomputing capacity for detailed investigations. It is noted that for the solidification problems, some of the major driving forces of the convection effect are from the temperature and/or solute gradients of the liquid phase These body force terms are almost invariably treated in the explicit manner in numerical computations. For large thermal or solutal Rayleigh numbers, the body forces are dominant in the governing equations, which can cause extreme difficulties and prevent the numerical procedures from converging to a stable solution

In all of the above referenced published works, time dependent calculations were conducted With the inclusion of the unsteady terms in the momentum, energy and solute transport equations, evolution of the phase change characteristics with respect to time can be investigated From the computational point of view, perhaps more importantly, the unsteady terms are usually treated in an implicit manner, either by the backward Euler methods [9] or by the Crank–Nicolson method [12]. The inclusion of the unsteady terms can help stabilize the numerical stability by enhancing the contributions of the implicit parts However, in virtually all previous works except that of Christenson *et al* [7] and Keller and Bergman [14], the computations were terminated before asymptotically steady-state solutions were obtained due to the lack of computing resources Hence the important questions related to steady-state behavior of the transport characteristics in a continuous solidification/melting process cannot be investigated Furthermore, very few works, with the exception of Brown's [11], have attempted to conduct studies of the solidification processes by systematically varying the controlling parameters

The present work attempts to elucidate the steady-state transport characteristics of the solidification process in a systematic way With the use of the Darcy law in the momentum equations to account for the presence of the mushy zone and with the use of the

NOMENCLATURE

A	constant in Darcy resistance (equation (9))
C	constant in Darcy resistance (equation (9))
C_p	specific heat
D	length of the domain
$f(T)$	function relating latent heat release and temperature
g	gravitational acceleration
Gr	Grashof number
H	total enthalpy
ΔH	latent heat release
J	Jacobian of inverse coordinate transformation as defined in equation (5b)
L	latent heat of phase change
p	pressure
Pr	Prandtl number
q_1, q_2, q_3	geometric relations between coordinates systems (equation (5b))
Ra	Rayleigh number
St	Stefan number
T	temperature
u, v	x, y velocity components
U, V	contravariant velocity components along ξ and η coordinates
x, y	Cartesian coordinates
$x_\xi, y_\eta, x_\eta, y_\xi$	metric coefficients of coordinate transformation

Greek symbols

α	thermal diffusivity of liquid
β	thermal expansion coefficient of liquid
λ	porosity
ν	kinematic viscosity
ξ, η	curvilinear coordinates
ϕ	sensible enthalpy

Subscripts

C	cold
H	hot
ℓ	liquidus phase
s	solidus phase
ξ, η	partial derivative with respect to ξ, η

Other symbol

$\bar{}$	dimensional quantity

enthalpy formulation, a unified set of steady-state equations governing the mass continuity, momentum, and energy transport are solved for all phases The controlling parameters, including the Rayleigh number, the Prandtl number, and the Stefan number are varied to investigate their impacts on the transport process. The size of the mushy zone as well as its influence on the solidification process is also studied by varying the temperature ranges within which the mushy zone exists

2. NUMERICAL FORMULATION

We have utilized the two-dimensional Navier–Stokes equations, including the mass continuity, momentum and energy equations, with the following treatments

(1) Boussinesq approximation for the density variation,

(2) Darcy law modeling of the effect of the mushy region between solid and liquid,

(3) enthalpy formulation [4–6] instead of temperature formulation for the energy equation

The enthalpy formulation alleviates the need for explicitly tracking the phase boundaries, but introduce extra source terms arising from the release of latent heat which can make the computation more difficult to converge We have developed the numerical methods capable of accounting for the above described physical models in the framework of the general curvilinear coordinates An adaptive grid computational technique has also been utilized to better resolve the flow characteristics

In terms of the non-dimensionalization procedure, the length of the whole domain, $\bar{D}$, thermal diffusivity of the liquid phase, $\bar{\alpha}$, specific heat, $\bar{C}_p$, and temperature differences between the right (hot) and left (cold) walls, $(\bar{T}_H - \bar{T}_C)$, are used as the reference physical quantities. Hence, the reference velocity and enthalpy scales are, respectively, $\bar{\alpha}/\bar{D}$ and $\bar{C}_p(\bar{T}_H - \bar{T}_C)$. The set of governing equations are given below in dimensionless form.

Continuity

$$\frac{\partial U}{\partial \xi} + \frac{\partial V}{\partial \eta} = 0 \tag{1}$$

u-Momentum

$$\frac{1}{J}\frac{\partial (Uu)}{\partial \xi} + \frac{1}{J}\frac{\partial (Vu)}{\partial \eta} = \frac{Pr}{J}\left[\frac{\partial}{\partial \xi}\left(\frac{1}{J}\left(q_1\frac{\partial u}{\partial \xi} - q_2\frac{\partial u}{\partial \eta}\right)\right) + \frac{\partial}{\partial \eta}\left(\frac{1}{J}\left(-q_2\frac{\partial u}{\partial \xi} + q_3\frac{\partial u}{\partial \eta}\right)\right)\right] - \frac{1}{J}\left[y_\eta\frac{\partial p}{\partial \xi} - y_\xi\frac{\partial p}{\partial \eta}\right] + Au \tag{2}$$

v-Momentum

$$\frac{1}{J}\frac{\partial(Uv)}{\partial\xi}+\frac{1}{J}\frac{\partial(Vv)}{\partial\eta}=\frac{Pr}{J}\left[\frac{\partial}{\partial\xi}\left(\frac{1}{J}\left(q_1\frac{\partial v}{\partial\xi}-q_2\frac{\partial v}{\partial\eta}\right)\right)+\frac{\partial}{\partial\eta}\left(\frac{1}{J}\left(-q_2\frac{\partial u}{\partial\xi}+q_3\frac{\partial v}{\partial\eta}\right)\right)\right]-\frac{1}{J}\left[x_\xi\frac{\partial p}{\partial\eta}-x_\eta\frac{\partial p}{\partial\xi}\right]+Ra\cdot Pr\cdot\phi+Av. \quad (3)$$

Energy equation based on sensible enthalpy (ϕ) and latent heat (ΔH)

$$\frac{1}{J}\frac{\partial(U\phi)}{\partial\xi}+\frac{1}{J}\frac{\partial(V\phi)}{\partial\eta}=\frac{1}{J}\left[\frac{\partial}{\partial\xi}\left(\frac{1}{J}\left(q_1\frac{\partial\phi}{\partial\xi}-q_2\frac{\partial\phi}{\partial\eta}\right)\right)+\frac{\partial}{\partial\eta}\left(\frac{1}{J}\left(-q_2\frac{\partial\phi}{\partial\xi}+q_3\frac{\partial\phi}{\partial\eta}\right)\right)\right]-\frac{1}{J\cdot St}\left[\frac{\partial}{\partial\xi}(U\cdot\Delta H)+\frac{\partial}{\partial\eta}(V\cdot H)\right] \quad (4)$$

where u, v are the Cartesian velocity components along the x- and y-directions, and U, V the contravariant velocity components along the ξ- and η-directions. Their relationships are as follows

$$U=uy_\eta-vx_\eta$$
$$V=vx_\xi-uy_\xi \quad (5a)$$

and the metrics are defined as

$$q_1=x_\eta^2+y_\eta^2$$
$$q_2=x_\xi x_\eta+y_\xi y_\eta$$
$$q_3=x_\xi^2+y_\xi^2$$
$$J=x_\xi y_\eta-x_\eta y_\xi \quad (5b)$$

More details regarding the formulation in curvilinear coordinates can be found in ref [15] The Rayleigh number is defined, with the overbar designating the dimensional quantities, as

$$Ra=\frac{\bar g\bar\beta(\bar T_H-\bar T_C)\bar D^3}{\bar\nu\bar\alpha} \quad (6)$$

and the Prandtl number is

$$Pr=\frac{\bar\nu}{\bar\alpha} \quad (7)$$

where $\bar\nu$ and $\bar\alpha$ are, respectively, kinematic viscosity and thermal diffusivity, $\bar g$ the gravitational acceleration, $\bar\beta$ the thermal expansion coefficient of liquid, and $\bar D$ the dimension of the square domain By combining the Rayleigh and Prandtl numbers, the Grashof number, Gr, emerges as

$$Gr=\frac{Ra}{Pr} \quad (8)$$

In equations (2) and (3) the Darcy law is invoked by assigning the terms Au and Av, where

$$A=\frac{-\bar C(1-\lambda)^2}{\lambda^3}\cdot\frac{\bar D^2}{\bar\alpha} \quad (9)$$

with λ being the porosity which is equal to 1 in liquid, 0 in solid, and varies continuously in the mushy zone between the two phases. With the pure liquid phase, the permeability is infinity and Darcy terms in the momentum equations reduce to the standard form of the Navier–Stokes formulation. The value of $\bar C\cdot\bar D^2/\bar\alpha$ is assigned here as $1.6\times10^3/Pr$, the same as in ref [9]

The energy equation, equation (4), is derived by splitting the total enthalpy of the material, H, into the sensible enthalpy, ϕ, and latent heat, ΔH, i e.

$$H=\phi+\Delta H \quad (10)$$

Within the mushy zone, the latent heat is considered as a function of temperature, T

$$\Delta H=f(T) \quad (11)$$

Here for the purpose of developing an appropriate numerical framework, a simple linear relationship between H and T as adopted in ref [9] is used

$$f(T)=\begin{cases}1, & T\geqslant T_\ell\\ \left(\dfrac{T-T_s}{T_\ell-T_s}\right), & T_\ell\geqslant T\geqslant T_s\\ 0, & T<T_s\end{cases} \quad (12)$$

where T_ℓ and T_s are, respectively, liquidus and solidus temperatures.

In equation (4), the dimensionless parameter associated with the phase change is the Stefan number, defined as

$$St=\frac{\bar C_p(\bar T_H-\bar T_C)}{\bar L} \quad (13)$$

where $\bar L$, $\bar C_p$, and $\bar T_H$ and $\bar T_C$ are, respectively, latent heat of the liquid, specific heat of the material, and the boundary values of the temperature field associated with the hot and cold walls

The solution methodology [15–17] employs a semi-implicit iterative algorithm capable of solving the coupled equations in non-orthogonal curvilinear coordinates. Along with the coordinate transformation, the finite volume formulation has been adopted in order to accurately honor the physical conservation laws A combined use of the Cartesian velocity components and contravariant velocity components is derived in the numerical algorithm In the momentum equations the Cartesian velocity components are treated as the primary variables. In the continuity (pressure correction) equation the contravariant velocity components are first updated and then the D'yakonov iteration is used to yield the corresponding values between the contravariant and Cartesian velocity components in an efficient manner This algorithm has been assessed against a wide variety of flow problems, as summarized in ref [18], and has been found to work well in general

The staggered grid system [15] is employed to store

the dependent variables. The second-order central difference schemes are used to discretize all the terms in the governing equations except the convection terms which are approximated by the second-order upwind scheme [19]. We have combined the present numerical algorithm for solving the coupled set of transport equations with an adaptive grid method developed earlier [20–22] in order to help obtain the convergent solutions and resolve flow structures. This method is based on the concept of a multiple one-dimensional grid adaptation procedure and redistributes the mesh spacing according to the concept of equidistribution of a weighting function. The weighting function here is comprised of the contributions from the smoothness and the enthalpy gradient. Substantial improvements in both the accuracy and convergence rate of the numerical solution have been observed [20, 22]. In the present works, it has been found that with a high Rayleigh number the adaptive grid technique is essential in yielding a convergent solution.

Wide variations of the controlling parameters, including the Rayleigh number (from 10^3 to 10^7), the Prandtl number (from 1.49×10^{-2} to 1×10^3), and the Stefan number (from 0.2 to 2.0), have been adopted to study their effects on the transport pattern in the presence of the phase change. The size of the mushy zone has also been varied by changing the temperature range within which it exists.

3. RESULTS AND DISCUSSIONS

In the present work, the buoyancy-induced convection is considered to be caused by the temperature gradient alone.

A square is taken as the domain of interest. As shown in Fig. 1, the boundary conditions are (1) no slip for the velocity field on all sides, and (2) constant wall temperature on two vertical boundaries, i.e. $T_H = 1$ ($\phi_H = 1$) and $T_C = 0$ ($\phi_C = 0$), and zero normal gradient condition on two horizontal boundaries. Two sets of the values of the minimum liquidus, T_l, and maximum solidus temperatures, T_s, have been considered to investigate the impact of the size and shape of the mushy zone on the solidification process. The values of T_l and T_s are taken as either (1) 0.6 and 0.4, or (2) 0.52 and 0.48. That is, the temperature variation across the mushy zone, $T_l - T_s$, is either 0.2 or 0.04.

A non-uniform 81×81 grid distribution was adopted as the original nodal system. Based on this grid distribution, the adaptive grid procedure was conducted. To illustrate the effect of the Rayleigh number on the adaptive grid distribution, Fig. 2 shows the adaptive grid systems corresponding to $Pr = 10^3$, $St = 0.2$, $T_l - T_s = 0.2$, and $Ra = 10^4$–10^7. It is noted that with the original grid system, it is often difficult to obtain a convergent steady-state solution with the present range of parameters. With the use of the adaptive grids, the difficulties associated with obtaining steady-state solution can be partially overcome. We have computed the steady-state solutions for both $T_l - T_s = 0.2$ and 0.04. With smaller values of $T_l - T_s$, the mushy zone is thinner and the slope of the sensible enthalpy variations between the phases becomes higher, causing the numerical scheme more difficulty in reaching the steady-state solution. In the present work, hundreds to thousands of iterations may be needed, depending on the combination of the above mentioned dimensionless parameters. Both the

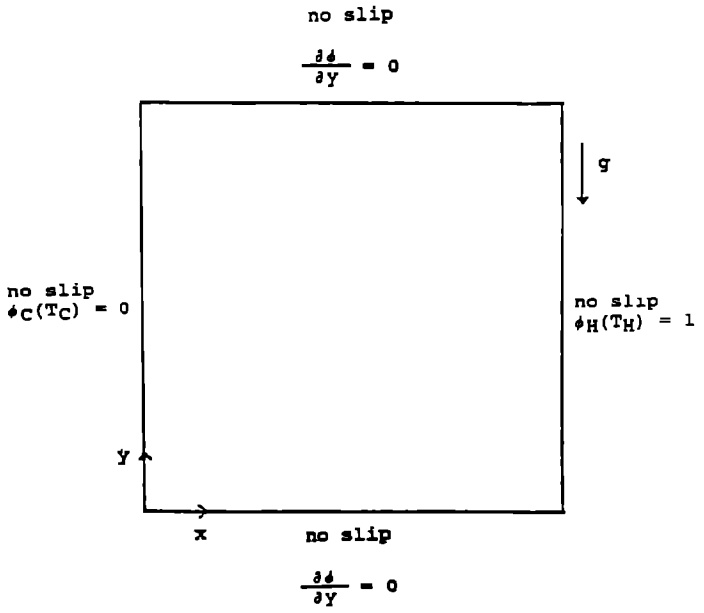

FIG. 1. Schematic of boundary conditions.

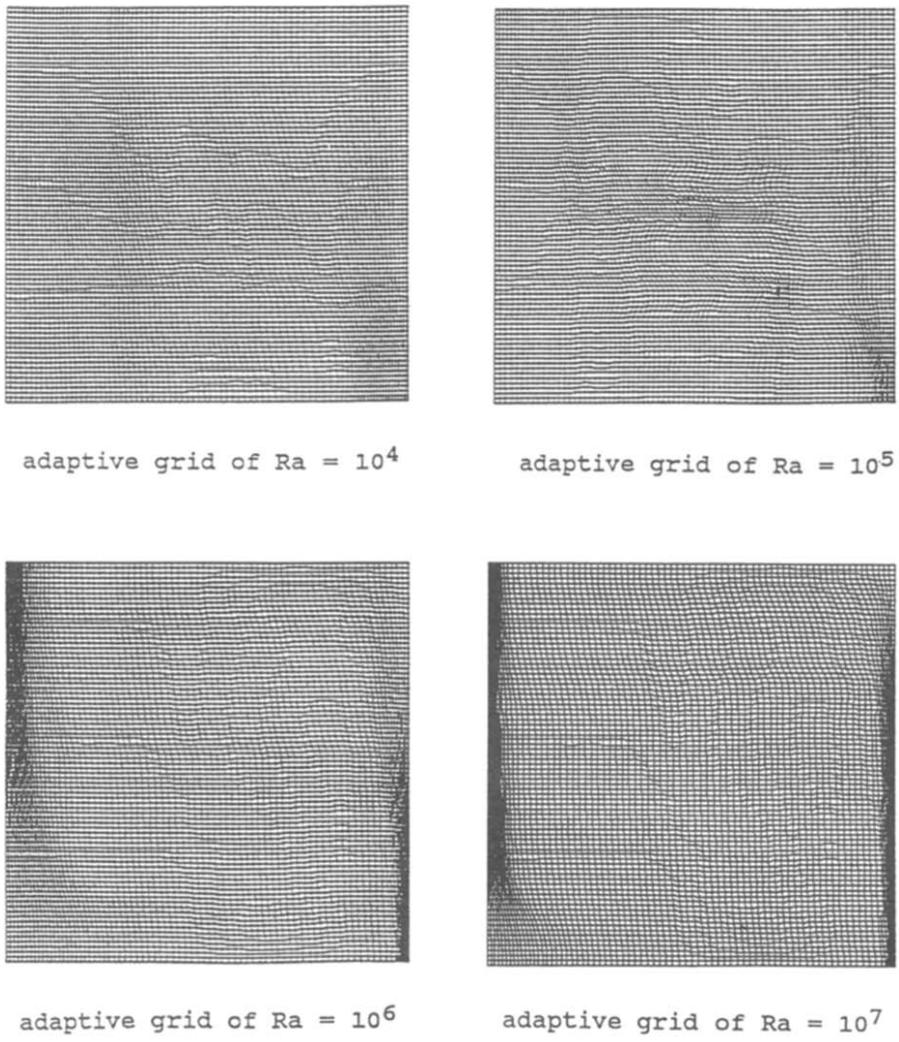

FIG 2 Illustration of adaptive grid systems for $Pr = 10^3$, $St = 0.2$, and $T_r - T_s = 0.2$

MicroVax 3100 and CRAY-XMP/48 computers have been employed for conducting the computation

3.1. $Pr = 10^1$, $St = 0.2$

Transient solutions for the case of $Pr = 10^1$, $St = 0.2$, and $Ra = 10^4$ have been reported by Voller and Prakash [9], and by Dantzig [12]. Because of the large Pr, the corresponding Grashof number for the case solved in refs. [9, 12] is only 10. Here we have obtained the steady-state solutions for a wider range of Ra than those previously employed. We have studied the solutions with Ra from 10^4 to 10^7.

3.1.1 $T_r - T_s = 0.2$. Figures 3–5 compare the streamlines, enthalpy contours, and phase variations for four different values of Ra, from 10^4 to 10^7, with $T_r - T_s = 0.2$. As the Rayleigh number increases, the mushy zone becomes thinner in the top region and thicker in the lower region. The pure liquid pool increases its width but decreases its depth as Ra increases. The shape of the interface is highly affected by the convection strength. At $Ra = 10^4$, the convection effect is weaker and the enthalpy distribution is substantially affected by conduction. Hence the mushy zone is more aligned to the vertical boundaries. The solutions are qualitatively similar to the transient ones reported earlier [9, 12].

For $Ra = 10^5$, the convection strength is more than three times as strong as that for 10^4. Consequently, the enthalpy contours are more concentrated in the top left and lower right regions. The boundary of the mushy zone adjacent to the pure liquidus phase is highly distorted and is expected to affect the solidification dynamics and dendritic formation.

As Ra further increases, the enthalpy contours responsively become more concentrated and the convection effect is more vigorous. Hence the mushy zone in the top left region becomes thinner. The other observable phenomenon is that at $Ra = 10^4$, convection is effectively dampened by the mushy zone, the convection cell largely conforms its boundary to

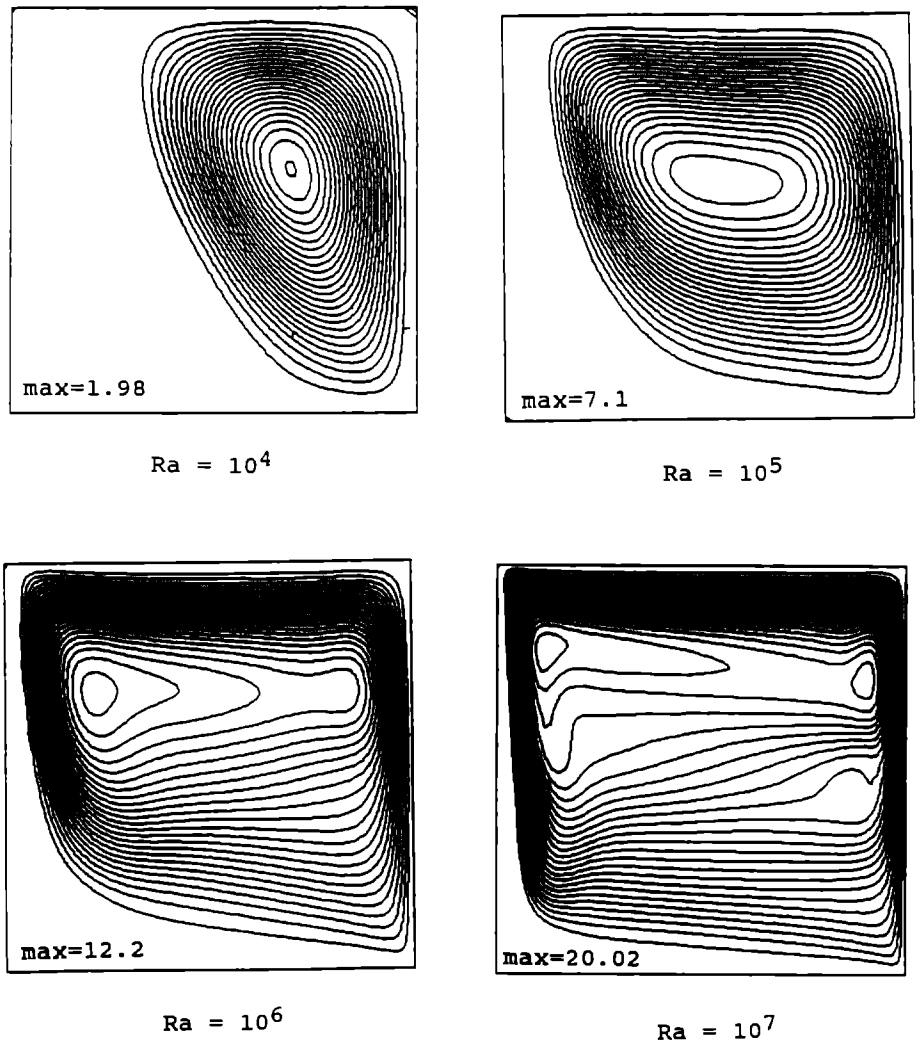

FIG 3 Streamlines of $Pr = 10^3$, $T_f - T_s = 0.2$, and $St = 0.2$

that of the mushy zone With increasing *Ra*, however, the convection becomes stronger and hence is able to penetrate more into the mushy zone At $Ra = 10^7$, despite the mushy zone being present in half of the domain, the convection cell occupies almost the whole region

The wiggling interface of $Ra = 10^5$ appears to result from the balance of convection and release of latent heat. The wiggles exist only within a range of *Ra* Similar interface characteristics have also been observed by Christenson *et al* [7] under different conditions. Both convection and latent heat release mechanisms are highly nonlinear and influence each other in a coupled manner The convection strength increases as *Ra* increases and hence is able to penetrate deeper into the mushy zone, causing the phase boundary to exert less influence on the transport characteristics As the Rayleigh (and Grashof) number further increases, the interface boundary again is of smoother shape The other observable phenomenon is that with increasing *Ra*, the streamfunction shifts its peak more toward the solid phase, eventually depicting a double-peak distribution

3 1 2 $T_f - T_s = 0.04$ By reducing $T_f - T_s$ from 0.2 to 0 04, the mushy zone becomes thinner with the same *Ra*, which produces a larger sensible enthalpy gradient between the two phases. Figure 6 shows the phase variations of $Ra = 10^4$ and 10^5, for both $T_f - T_s = 0.2$ and 0 04 Because the overall dynamic process is nonlinear, the locations of the mushy zone do not coincide with each other as $T_f - T_s$ changes

Figure 7 shows the enthalpy contours and streamlines of the corresponding cases with $T_f - T_s = 0.04$. As $T_f - T_s$ is reduced, the mushy zone occupies a smaller portion of the domain and hence the size of the liquid pool becomes larger By comparing Fig 3 and Fig. 7(b), the enthalpy contours are less concentrated for the cases of smaller values of $T_f - T_s$ The streamfunctions, on the other hand, appear relatively insensitive to the change of $T_f - T_s$

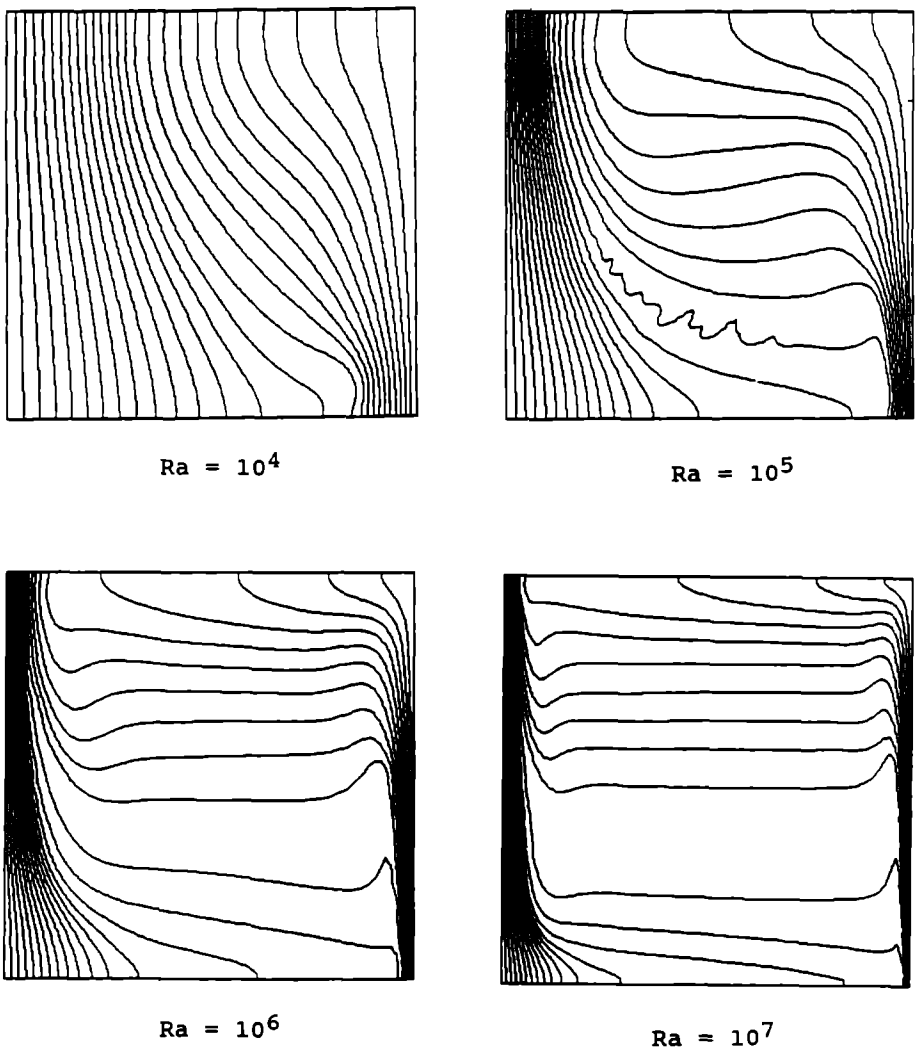

FIG 4 Enthalpy contours of $Pr = 10^3$, $T_f - T_s = 0.2$, and $St = 0.2$, contour interval = 0.0385

3.2 *Effect of Prandtl number*

3.2.1. $Pr = 1.49 \times 10^{-2}$, $St = 0.2$, $T_f - T_s = 0.2$. By reducing the Prandtl number from 10^3 to 1.49×10^{-2}, the Grashof number increases by a factor of 6.7×10^4 for the same Rayleigh number. Since the controlling parameter governing the relative dominance of the convection vs viscous terms in the momentum equations is $\sqrt{(Gr)}$, the fluids of lower Prandtl number depict much stronger non-linear characteristics than those of high Prandtl number. This change of fluid properties causes the numerical algorithm to experience much more difficulties in yielding the convergent steady-state solutions. With $Pr = 1.49 \times 10^{-2}$ and $St = 0.2$, no solutions, by using either the first- or second-order upwind schemes for the convection terms, can be obtained for the Rayleigh number of 10^6, which corresponds to $Gr = 6.7 \times 10^7$. Obviously the source terms associated with the phase change increase the nonlinearity of the governing equations and hence make the problems more difficult to solve. For the single phase flow, steady-state solutions with the identical numerical treatments as well as by using the identical number of nodal points have been successfully computed for the same Pr [23].

Figures 8–10 compare the solutions of $Pr = 1.49 \times 10^{-2}$, $St = 0.2$, and $T_f - T_s = 0.2$ for three different Rayleigh numbers, 10^3, 10^4, and 10^5. Similar to the cases of $Pr = 10^3$, both the strength and size of the convection eddy increase as Ra increases. As expected, with almost five orders of magnitude difference in Pr, the enthalpy distributions, the resulting shapes of the convection cell, as well as the locations of the phase boundaries, change noticeably as Pr varies from 10^3 to 1.49×10^{-2}. Since the enthalpy field is under much stronger conduction influence with $Pr = 1.49 \times 10^{-2}$ than with $Pr = 10^3$, the location of the mushy zone is now closer to the middle of the domain. In this regard, it should be noted that two competing factors are at work. With the same size of liquid pool, the lower Pr fluids tend to develop a

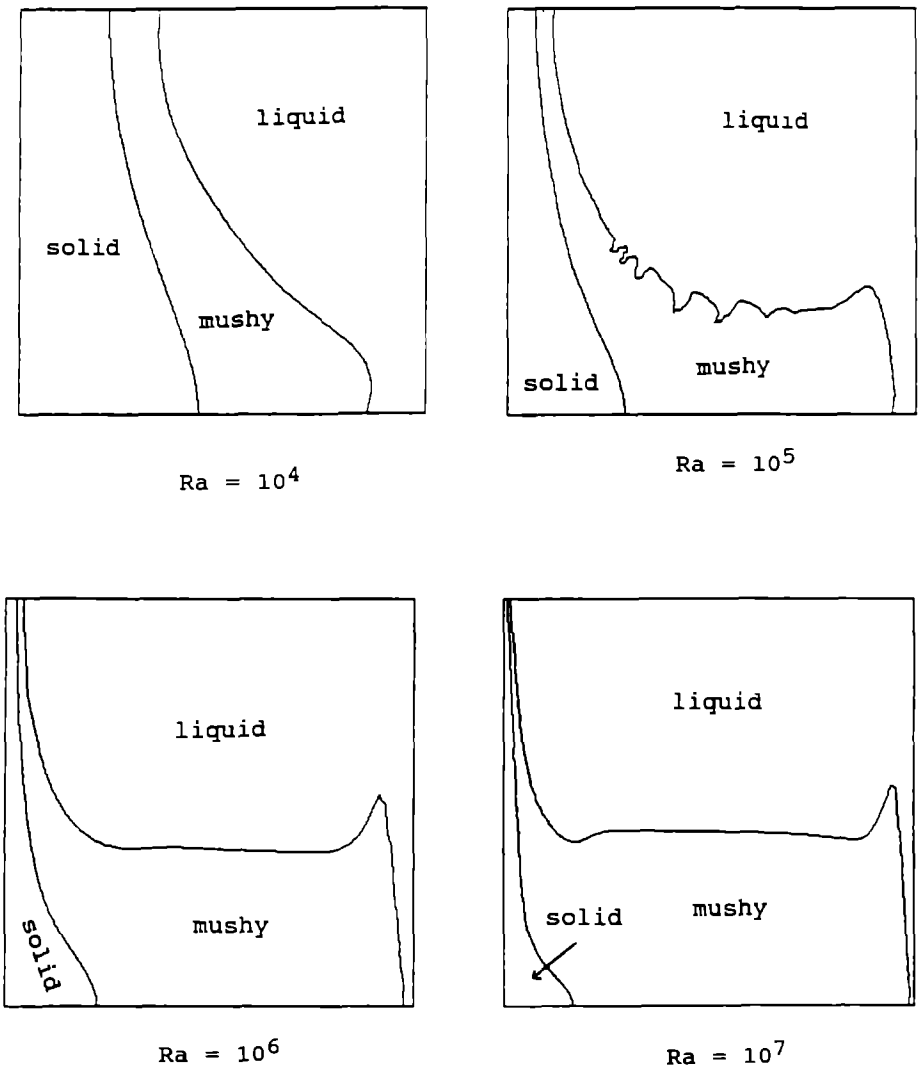

FIG 5 Phase variations of $Pr = 10^3$, $T_r - T_s = 0.2$, and $St = 0.2$

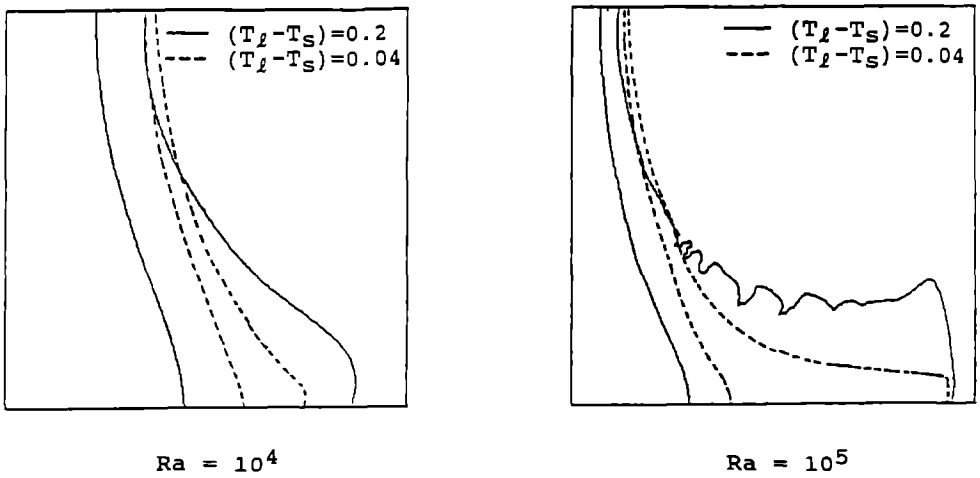

FIG 6 Comparison of phase variations of $Pr = 10^3$, $St = 0.2$, and $T_r - T_s = 0.2$ and 0.04, respectively

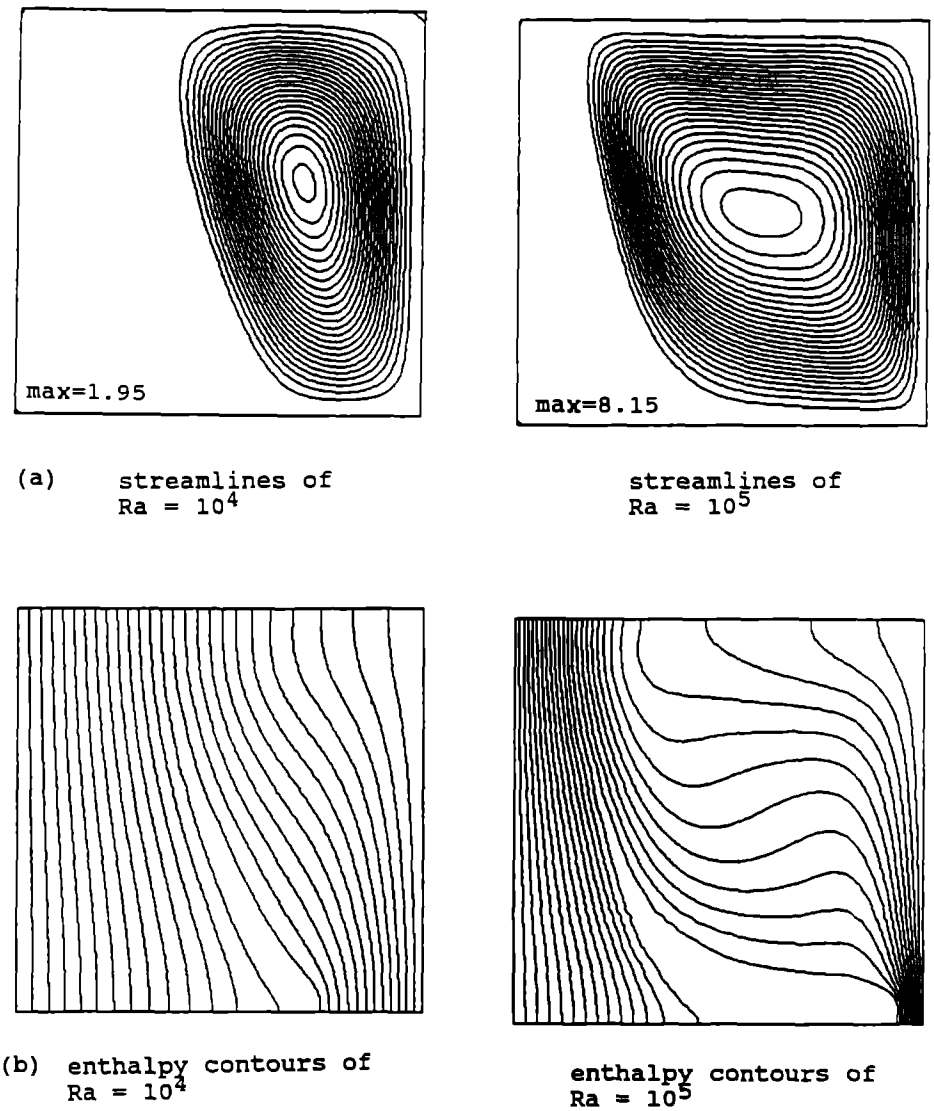

FIG 7 Streamlines and enthalpy contours of $Pr = 10^3$, $St = 0.2$, and $T_f - T_s = 0.04$

stronger convection effect for the same Ra (which results in high Gr) However, extra complexities are introduced by phase changes; lower Pr also causes the enthalpy contours to be less concentrated with the same Ra, resulting in a smaller size of the liquid pool Since Gr is dependent on the size of the liquid pool to the third power, the smaller size of the liquid pool reduces Gr Hence, overall convection strength is determined by the balance of the competing effects.

3 2.2. $Pr = 1$, $St = 0.2$, $T_f - T_s = 0.2$. Figures 11–13 show the solutions for the cases of $Ra = 10^4$–10^6 with $Pr = 1\ 0$. By combining with other cases of identical Ra, St, $T_f - T_s$, but different Pr, it can be observed that the solutions experience an evolutionary change of characteristics as Pr varies from a smaller value to a larger value With $Pr = 10^3$, the wiggling phase boundary appears at $Ra = 10^5$. As shown in Fig 13, with $Pr = 1$, the wiggles do not appear until $Ra = 10^6$ The magnitudes of the wiggles are also smaller for $Pr = 1$ than for $Pr = 10^1$ Since the length scale of the enthalpy field is proportional to $(Pr/Gr)^{-1/2}$, reduction of Pr causes the length scale in the enthalpy field to increase Hence the enthalpy contours of lower Pr fluids become more smoothly distributed, causing the wiggling phase boundaries to disappear

3 3 *Effect of Stefan number*

The Stefan number characterizes the relative magnitude of the source term in the energy equation introduced by the release of latent heat in the course of solidification. The results presented so far are with $St = 0.2$. Calculations have also been conducted for $St = 2\ 0$ with $Pr = 1.49 \times 10^{-2}$ and 10^1. the solutions are presented in the following sections.

3 3.1. $Pr = 1.49 \times 10^{-2}$, $St = 2\ 0$, $T_f - T_s = 0\ 2$.

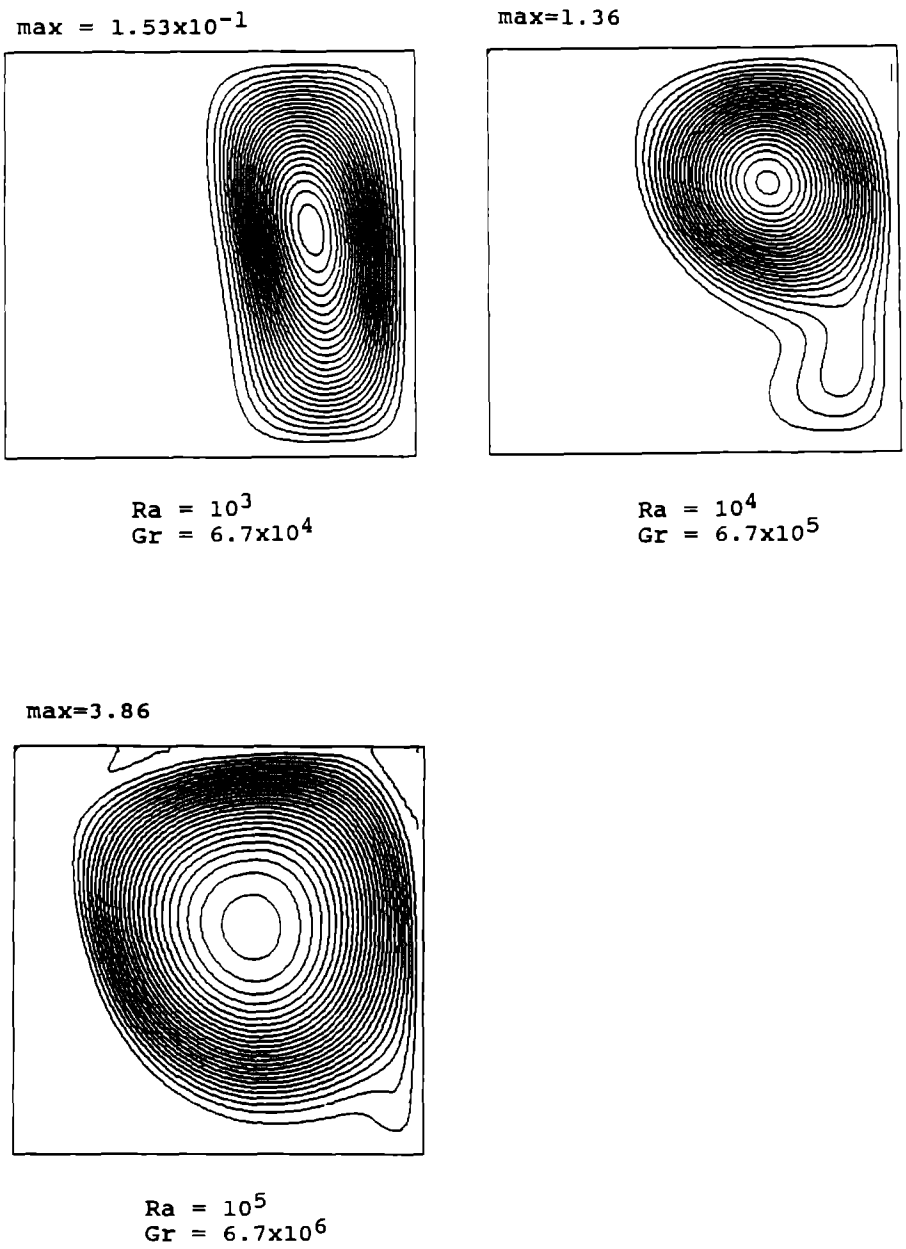

FIG 8 Streamlines of $Pr = 1.49 \times 10^{-2}$, $T_\ell - T_s = 0.2$, and $St = 0.2$

Figure 14 compares the solution with $Pr = 1.49 \times 10^{-2}$, $St = 2.0$, and $T_\ell - T_s = 0.2$ for two different Rayleigh numbers, $Ra = 10^4$ ($Gr = 6.7 \times 10^5$) and 10^5 ($Gr = 6.7 \times 10^6$). As expected, the relative effect of the Rayleigh number on the transport characteristics remains the same. However, by comparing the solutions of $St = 2.0$ (Fig. 14) to those of $St = 0.2$ (Figs. 8–10), one can clearly discern the impact of St on the enthalpy as well as the convection pattern. With higher St, the effect of the latent heat on the enthalpy equation is reduced. Consequently, the interface between the mushy region and the pure liquid region becomes less distorted with the same values of Ra and Pr. Figure 14(c) compares the effects of St on the shape and location of the mushy zone, large impacts have been observed. With regard to the velocity field, higher values of St cause the convection cells to shrink in size.

3.3.2. $Pr = 10^{-1}$, $Ra = 10^4$, $St = 2.0$. Figure 15 shows the solutions with $St = 2.0$, $Pr = 10^{-1}$, and $Ra = 10^4$. Two values of $T_\ell - T_s$ have been tested, namely, 0.2 and 0.04. Inspections of the enthalpy contours shown in Figs. 4 (for $T_\ell - T_s = 0.2$, $St = 0.2$), 7(b) (for $T_\ell - T_s = 0.04$, $St = 0.2$), and 15(b) (for $St = 2.0$) reveal that higher St causes the enthalpy field to depict smoother distribution. An increase in

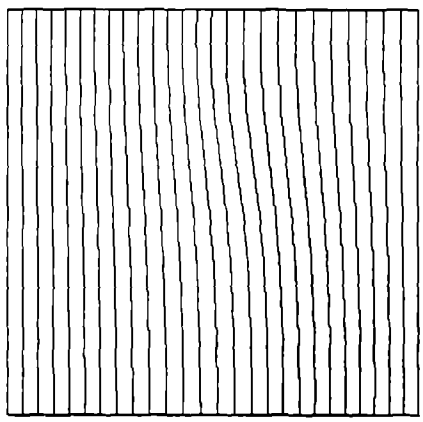

Ra = 10^3
Gr = 6.7×10^4

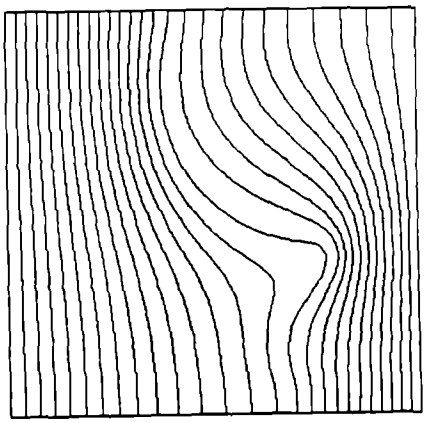

Ra = 10^4
Gr = 6.7×10^5

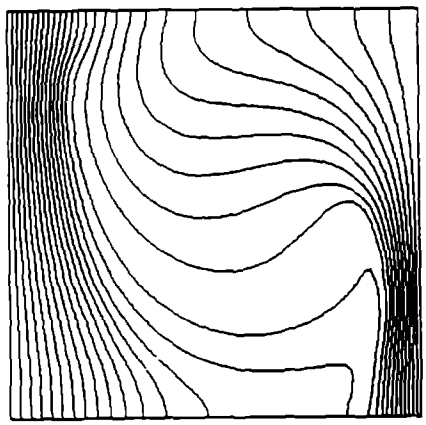

Ra = 10^5
Gr = 6.7×10^6

FIG 9 Enthalpy contours of $Pr = 1.49 \times 10^{-2}$, $T_f - T_s = 0.2$, and $St = 0.2$.

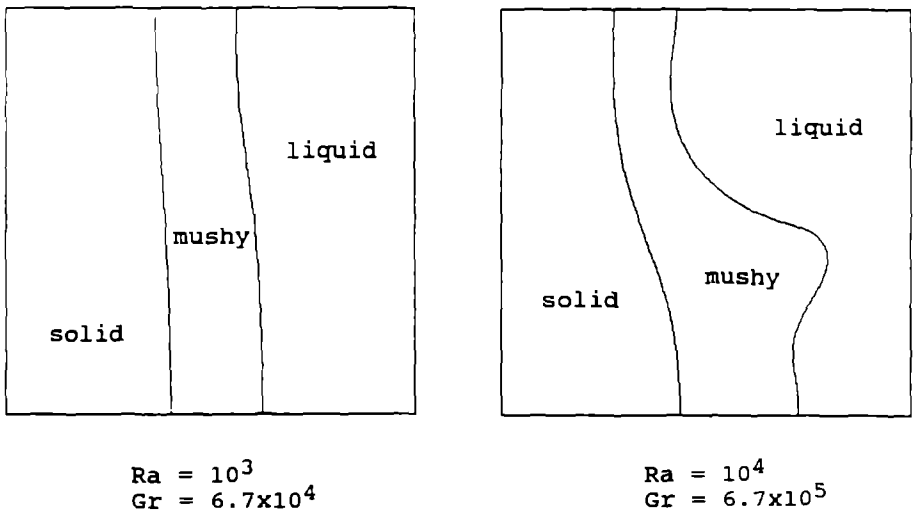

FIG. 10 Phase variations of $Pr = 1.49 \times 10^{-2}$, $T_f - T_s = 0.2$, and $St = 0.2$

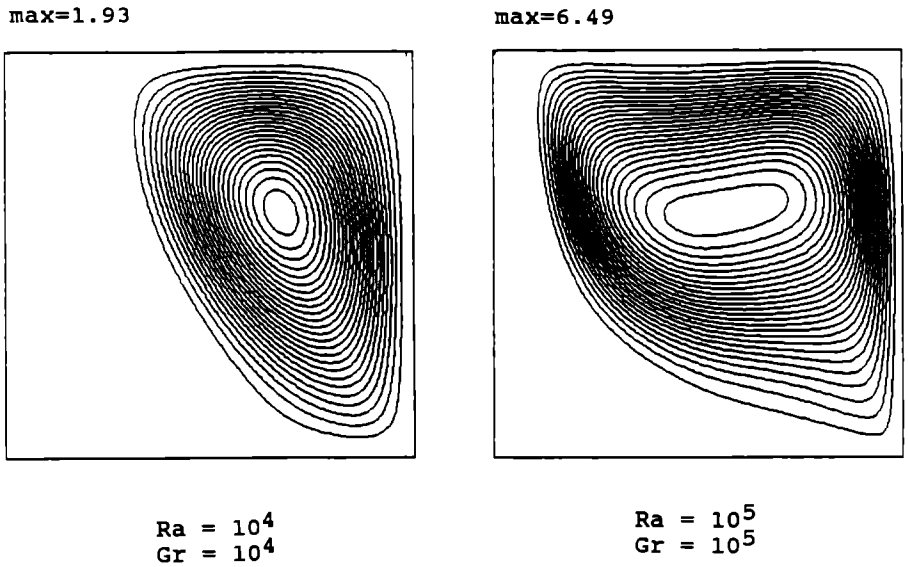

FIG 11 Streamlines of $Pr = 1$, $T_f - T_s = 0.2$, and $St = 0.2$

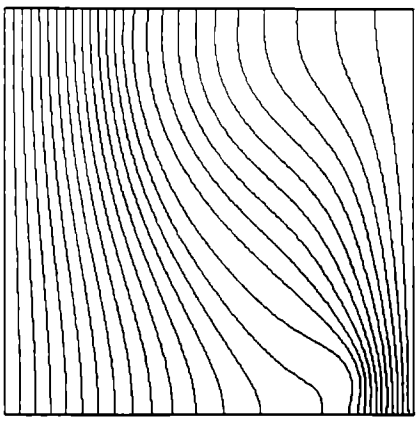

$Ra = 10^4$
$Gr = 10^4$

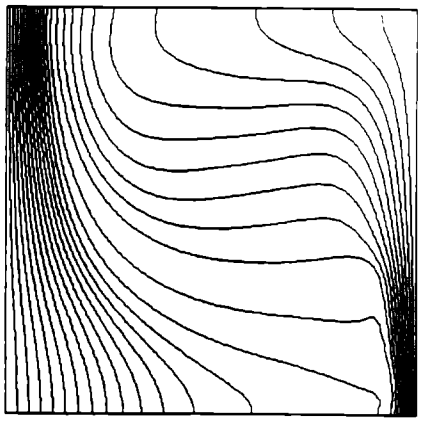

$Ra = 10^5$
$Gr = 10^5$

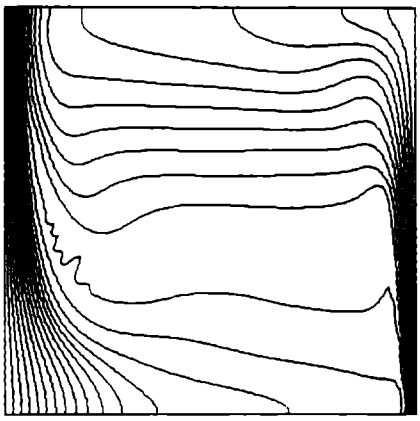

$Ra = 10^6$
$Gr = 10^6$

FIG. 12 Enthalpy contours of $Pr = 1$, $T_c - T_s = 0.2$, and $St = 0.2$

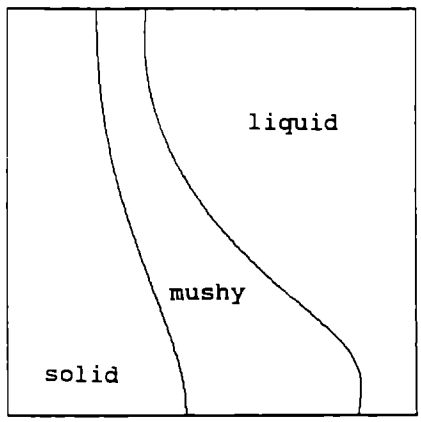

$Ra = 10^4$
$Gr = 10^4$

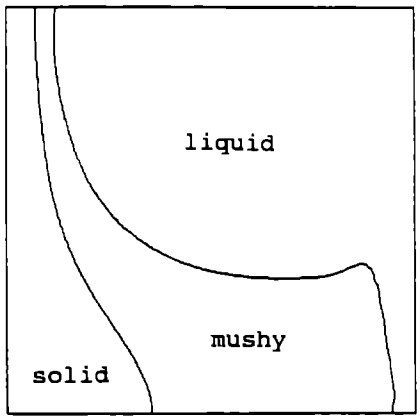

$Ra = 10^5$
$Gr = 10^5$

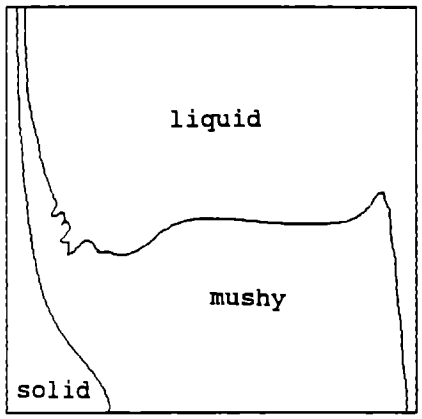

$Ra = 10^6$
$Gr = 10^6$

FIG 13 Phase variations of $Pr = 1$, $T_r - T_s = 0.2$, and $St = 0.2$

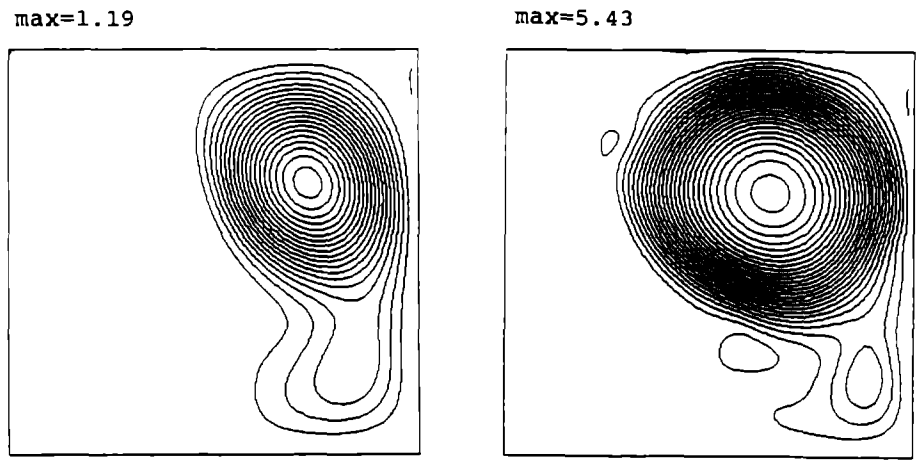

Ra = 10^4 Ra = 10^5

(a) streamlines, St = 2.0.

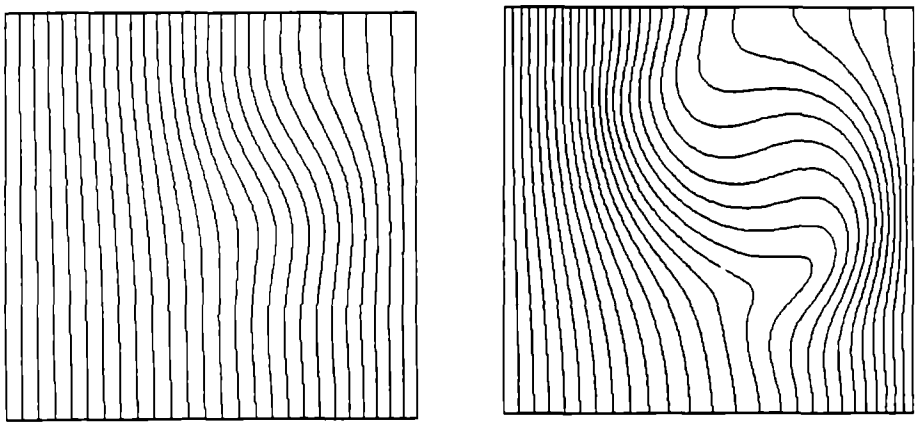

Ra = 10^4 Ra = 10^5

(b) enthalpy contours, St = 2.0.

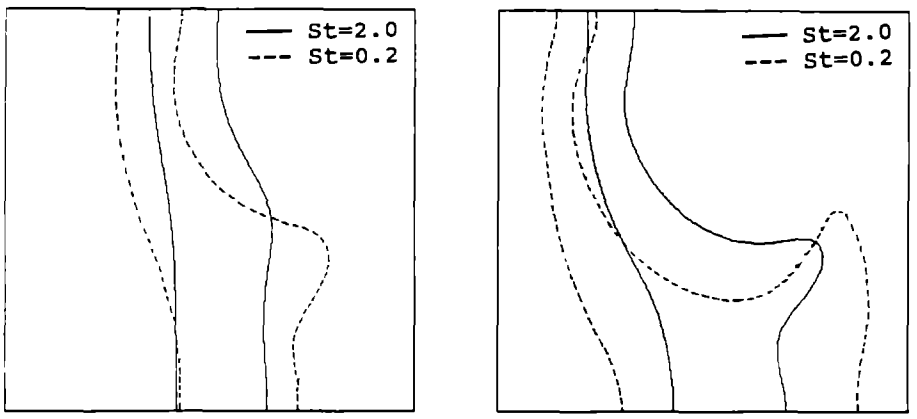

Ra = 10^4 Ra = 10^5

(c) phase variations

FIG 14 Transport characteristics for $Pr = 1.49 \times 10^{-2}$ and $T_f - T_s = 0.2$

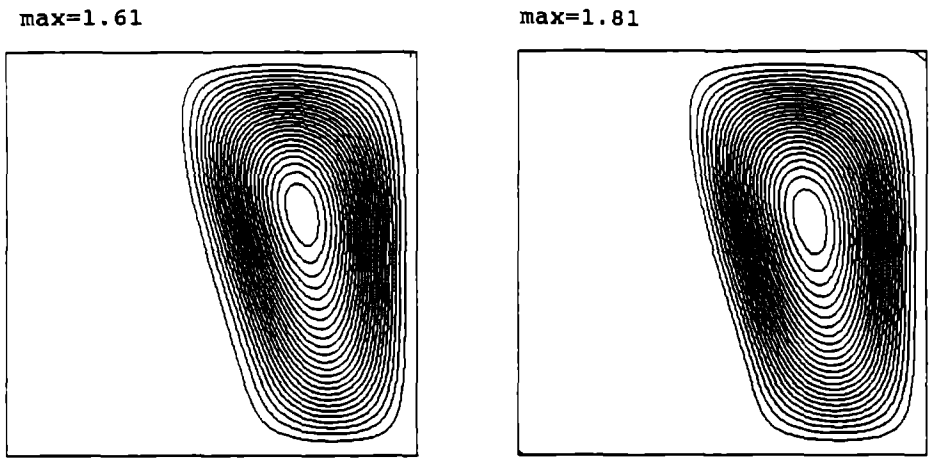

$T_\ell - T_S = 0.2$ $T_\ell - T_S = 0.04$

(a) streamlines, St = 2.0.

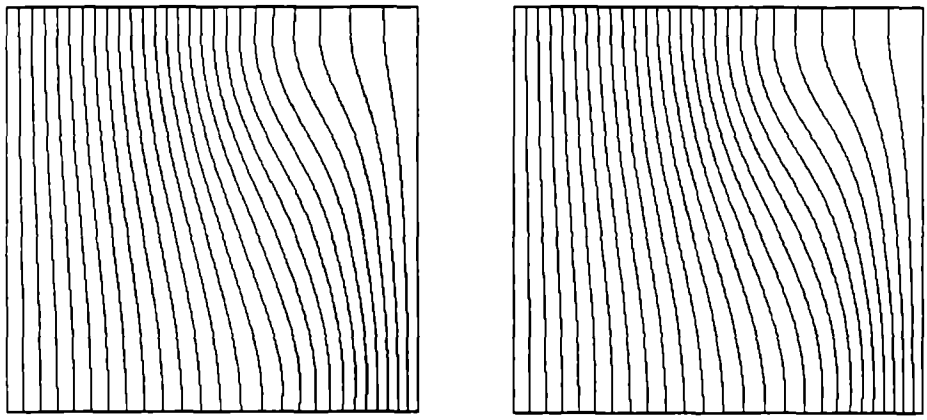

$T_\ell - T_S = 0.2$ $T_\ell - T_S = 0.04$

(b) enthalpy contours, St = 2.0.

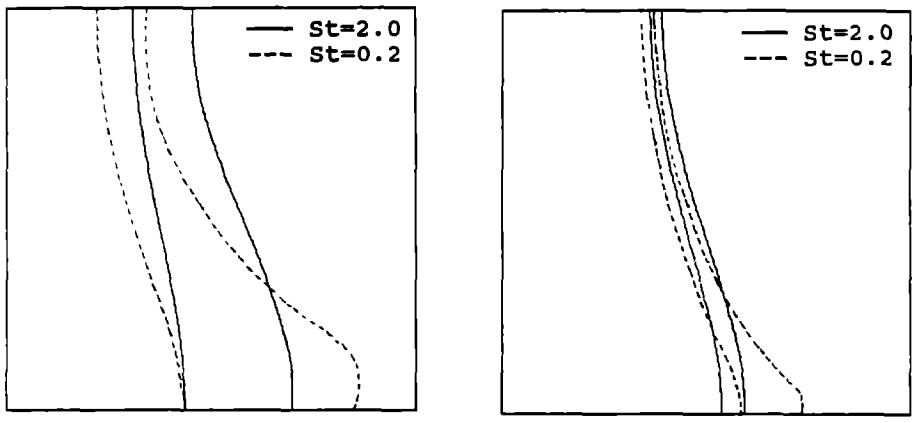

$T_\ell - T_S = 0.2$ $T_\ell - T_S = 0.04$

(c) phase variations, St = 2.0.

FIG 15 Transport characteristics for $Pr = 10^3$ and $Ra = 10^4$

St also makes the mushy zone less distorted and move more toward the middle of the domain These changes of distribution in both the temperature field and the mushy zone shape show corresponding influence on the convection field as one can observe by comparing Figs 3, 7(a), and 15(a)

4 SUMMARY AND CONCLUSION

Based on the preceding discussions and the results presented, the following conclusions can be reached

(1) Steady-state solutions have been successfully obtained for many different combinations of controlling parameters

(2) The size and strength of the convection cell increase as *Ra* increases Higher *Ra* causes the mushy zone to exhibit more distorted phase boundaries

(3) With increasing *Ra*, the location of peak values of the streamfunction moves toward the solid. Eventually a double-peak distribution of the streamfunction appears with high *Ra* cases for $Pr = 1$ and 10^3.

(4) The reduction of $T_f - T_s$ makes the mushy region change location as well as thickness. The wiggling shape of the phase boundary also disappears as $T_f - T_s$ decreases

(5) The Prandtl number exerts a complicated influence on the transport pattern With fixed *Ra*, lower *Pr* causes *Gr* (and the convection strength) to increase, it also promotes a smoother enthalpy field, which produces a smaller liquid pool The resulting convection field is balanced by these competing factors

(6) The Stefan number exhibits a substantial influence on the shape of the interface A lower Stefan number, i e. higher relative value of the latent heat release, causes the phase boundary to be more distorted

Acknowledgement—Some of the computations were made using CRAY-XMP/48 of the National Center for Supercomputer Applications (NCSA) at the University of Illinois through a research grant

REFERENCES

1 M C. Flemings, *Solidification Processing* McGraw-Hill, New York (1974)
2 M E Glicksman, S R Coriell and G B McFadden, Interaction of flows with the crystal–melt interface, *Ann Rev. Fluid Mech.* **18,** 307–335 (1986)
3 S Ganesan and D R Poirier, Conservation of mass and momentum for the flow interdendritic liquid during solidification, *Metall Trans B* **21,** 173–181 (1990)
4 L S Yao and J Prusa, Melting and freezing In *Advances in Heat Transfer* (Edited by J P Hartnett and T F Irvine), Vol 19, pp 1–95 Academic Press, New York (1989)
5 J Crank, *Free and Moving Boundary Problems* Oxford University Press, Oxford (1984)
6 R Viskanta, Heat transfer during melting and solidification of metals, *ASME J Heat Transfer* **110,** 1205 1219 (1989)
7 M S Christenson, W D Bennon and F P Incropera, Solidification of an aqueous ammonium chloride solution in a rectangular cavity—II Comparison of predicted and measured results *Int J Heat Mass Transfer* **32,** 69–79 (1989)
8 C Beckermann and R Viskanta, Double-diffusive convection due to melting, *Int J Heat Mass Transfer* **31,** 2077–2089 (1988)
9 V R Voller and C Prakash, A fixed grid numerical modeling methodology for convection-diffusion mushy region phase-change problems, *Int J Heat Mass Transfer* **30,** 1709–1719 (1987)
10 M E Thompson and J Szekely, Mathematical and physical modeling of double-diffusive convection of aqueous solution crystallizing at a vertical wall *J Fluid Mech* **187,** 409–433 (1988)
11 R A Brown, Theory of transport processes in single crystal growth from the melt, *A I Ch E Jl* **34,** 881–911 (1988)
12 J A Dantzig, Modeling liquid–solid phase change with melt convection, *Int J Numer Meth Engng* **28,** 1769–1785 (1989)
13 J C Heinrich, S Felicelli, P Nadapukar and D R Poirier, Thermosolutal convection during dendritic solidification of alloys, part II nonlinear convection, *Metall Trans B* **20,** 883–891 (1989)
14 J R Keller and T L Bergman, Prediction of conjugate heat transfer in a solid–liquid system inclusion of buoyancy and surface tension forces in the liquid phase, *ASME J Heat Transfer* **111,** 690–698 (1989)
15 W Shyy, S S Tong and S M Correa, Numerical recirculating flow calculation using a body-fitted coordinate system, *Numer Heat Transfer* **8,** 99–113 (1985)
16 M E Braaten and W Shyy, a study of recirculating flow computation using body-fitted coordinates consistency aspects and mesh skewness, *Numer Heat Transfer* **9,** 559–574 (1986)
17 W Shyy, S W Correa and M E Braaten, Computation of flow in a gas turbine combustor, *Combust Sci Technol* **58,** 97–117 (1988)
18 W Shyy and T C Vu, On the adoption of velocity variable and grid system for fluid computation in curvilinear coordinates, *J Comput. Phys* (1990), in press
19 W Shyy, A study of finite difference approximations to steady-state, convection-dominated flow problems, *J Comput Phys* **57,** 415–438 (1985)
20 W Shyy, An adaptive grid method for Navier Stokes flow computation *Appl Math Comput* **21,** 201–219 (1987)
21 W Shyy, An adaptive grid method for Navier–Stokes flow computation, part II grid addition, *Appl Numer Math* **2,** 9–19 (1986)
22 W Shyy, Computation of complex fluid flows using an adaptive grid method, *Int J Numer Meth Fluids* **8,** 475–489 (1988)
23 W Shyy and M-H Chen, A study of transport process of buoyancy-induced and thermocapillary flow of motion alloy, AIAA Paper 90-0255, AIAA 28th Aerospace Sciences Meeting, Reno Nevada, 8–11 January (1990)

CONVECTION NATURELLE PERMANENTE AVEC CHANGEMENT DE PHASE

Résumé—La convection naturelle modifie significativement les mécanismes de transport pour un matériau expérimenté avec changement de phase On a calculé les solutions permanentes de la convection et les transferts associés de quantité de mouvement et d'énergie, en considerant simultanément les zones solide, liquide et mixte On utilise pour un large domaine de nombres de Rayleigh, Prandtl et Stefan, des techniques de volumes finis, avec coordonnées curvilignes non orthogonales, une discrétisation du second ordre, un nombre adéquat de points nodaux et une méthode de grille adaptative On trouve que la taille et l'intensite de la cellule convective, ainsi que la position et la forme des limites des phases sont toutes fortement dépendantes de la combinaison des paramètres de contrôle et du domaine de température qui gouverne l'existence de la zone mixte Une présentation systématique de l'effet de ces facteurs sur les caracteristiques du transport est faite pour dégager les mécanismes physiques responsables du changement de phase

STATIONÄRE NATÜRLICHE KONVEKTION MIT PHASENWECHSEL

Zusammenfassung—Die naturliche Konvektion beeinflußt die Transportvorgange beim Phasenwechsel eines Materials in signifikanter Weise. In der vorliegenden Arbeit werden die Impuls- und Energietransportgleichungen für stationare Konvektionsströmung unter Berücksichtigung der Feststoff-, Flussigkeits- und Erweichungszone gelöst Hierzu wird ein Finite-Volumina-Verfahren mit nichtorthogonalen krummlinigen Koordinaten, einer Diskretisierung 2 Ordnung, einer ausreichenden Anzahl von Knotenpunkten und einer angepaßten Gitterlosungsmethode verwendet. Es wird ein weiter Bereich der Rayleigh-, Prandtl- und Stefan-Zahl untersucht Es zeigt sich, daß die Größe und Starke der Konvektionszelle wie auch die Position und Form der Phasengrenzen stark von den oben angegebenen Kontrollparametern und vom Temperaturbereich abhängt, durch den die Existenz der Erweichungszone bestimmt wird Es wird der Einfluß dieser Faktoren auf die Transporteigenschaften systematisch dargestellt, um die physikalischen Mechanismen, die für den Phasenwechselprozeß verantwortlich sind, festzulegen

СТАЦИОНАРНАЯ ЕСТЕСТВЕННАЯ КОНВЕКЦИЯ ПРИ ФАЗОВОМ ПРЕВРАЩЕНИИ

Аннотация—Естественная конвекция оказывает существенное влияние на процессы теплопереноса при наличии фазовых превращений. В настоящей работе проведено численное исследование стационарной конвекции с учетом одновременного существования твердой, жидкой и пористой зон. Численный анализ выполняется в широком диапазоне чисел Рэлея, Прандтля и Стефана методом конечных элементов с использованием неортогональных криволинейных координат, дискретизации второго порядка, адекватного числа узловых точек и метода адаптивной сетки Установлено, что размер и интенсивность конвективной ячейки, а также расположение и форма фазовых границ зависят от комбинации перечисленных определяющих параметров и температурного диапазона существования пористой зоны. Для выявления физических механизмов фазовых превращений в статье детально рассмртрено влияние этих факторов на характеристики переноса